Materiales de Construcción
Vol. 74, Issue 355, July-September 2024, e353
ISSN-L: 0465-2746
https://doi.org/10.3989/mc.2024.371123

Effect of pre-wetting treatment for waste waterglass foundry sand on the properties of alkali-activated slag

X. Shen[a], P. Chen[a,b]✉, S. Li[a], Y. Wang[a], S. Hu[a], C. Pei[a], J. Xie[a]

[a] School of Civil Engineering and Architecture, Anhui University of Science and Technology, (Huainan, P.R. China)
[b] State Key Laboratory of Mining Response and Disaster Prevention and Control in Deep Coal Mines, Anhui University of Science and Technology, Huainan, (Anhui, P.R. China)
✉: peiyuan29@126.com

Received 22 December 2023
Accepted 27 April 2024
Available on line 4 November 2024

ABSTRACT: Waste waterglass foundry sand (WwFS) is a solid waste generated by the foundry industries that is commonly discarded in landfills and has urgent needs for disposal and recycling. Accordingly, this study suggests using WwFS as aggregates source for the preparation of alkali-activated slag mortars (AASM). Two different pre-wetting methods (24 h pre-wetting at 20°C and 1~6 h pre-wetting at 70°C) were used to treat WwFS and compared their performances with adding quartz sand and dried WwFS mortars. Compared to WwFS mortars without pre-wetting treatment, the compressive strengths of WwFS mortars containing WwFS pre-wetting in water at 70°C at 28d were increased by 1.3~10.0%, and the C-(A)-S-H average elastic modulus was increased by 16%. This study confirmed the feasibility of using hot water pre-wetted WwFS as the single aggregate source for AASM, which is important for the large-scale utilization of WwFS.

KEY WORDS: Alkali-activated slag materials; Waste waterglass foundry sand; Interface; Compressive strength; Nanoindentation.

Citation/Citar como: Shen X, Chen P, Li S, Wang Y, Hu S, Pei C, Xie J. 2024. Effect of pre-wetting treatment for waste waterglass foundry sand on the properties of alkali-activated slag. Mater. Construcc. 74(355):e353. https://doi.org/10.3989/mc.2024.371123

RESUMEN: *Efecto del pretratamiento de humectación del residuo de arena procedente de la fundición de vidrio en las propiedades de la escoria activada alcalinamente*. La arena de fundición de vidrio lixiviado (WwFS, por sus siglas en inglés) es un residuo sólido generado por las industrias de fundición que comúnmente se desecha en los vertederos y tiene necesidades urgentes de eliminación y reciclaje. En consecuencia, este estudio sugiere utilizar WwFS como árido para la preparación de morteros de escoria activada alcalinamente (AASM). Se utilizaron dos métodos de prehumectación diferentes (24 h de prehumectación a 20 °C y 1 ~ 6 h de prehumectación a 70 °C) para tratar el WwFS y se comparó su comportamiento con el de morteros con arena de cuarzo y con WwFS seco. Las resistencias a la compresión de los morteros WwFS que contienen prehumectación WwFS en agua a 70 °C a 28 días aumentaron entre un 1,3 y un 10,0 % respecto a las obtenidas en los morteros WwFS sin tratamiento de humectación previa, y el módulo elástico promedio C-(A)-S-H aumentó un 16%. Este estudio confirmó la viabilidad de utilizar WwFS prehumedecidos con agua caliente como único árido para AASM, lo cual es importante para la utilización a gran escala de WwFS.

PALABRAS CLAVE: Materiales de escorias activadas alcalinamente; Residuo de arena procedente de la fundición de vidrio; Interfase; Resistencia a la compresión; Nanoindentación.

1. INTRODUCTION

With the increasing demand for machines and equipment around the world, the foundry industry is in a flourishing period. About 112.7 million tons of metal castings were produced worldwide in 2018 (1), and this figure will exceed 120 million tons in the next decade. Casting production generates a large amount of waste foundry sand (WFS), even if recycled in the production process, it still yields 600 kg of WFS per ton of casting produced (2). Normally, WFS is classified into green sand and chemically bonded foundry sand, the latter is quartz sand bound together by chemical binders such as waterglass, phenolic-urethanes, epoxy-resins and furfur alcohol (3-5). Over the years, WFS has been dumped in landfills (6-8) due to its high alkaline and toxic compounds (9-11) that bring high treatment cost, which further contributes to soil and groundwater pollutions (12, 13).

Therefore, the question of how to dispose of and utilize these hard-to-handle WFS, while minimizing their impact on the environment and the economy, has attracted considerable attention. Considering that WFS is harmful to mechanical properties and durability when used as a fine aggregate in cement systems (14-16), and that low utilization (10-30%) is an obstacle to the effective use of WFS in concrete (17, 18), several researchers chose to use WFS in alkali-activated slag mortars (AASM). For example, Ferrazzo et al. (7) found that substituting some of the sand with WFS, with sugar cane bagasse ash and hydrated eggshell lime as raw materials, AASMs were produced with higher strength, stiffness, and durability than ordinary Portland cement (OPC). Sabour et al. (19) demonstrated that, compared to cement-based mortar, AASM containing treated WFS exhibited a 158% increase in compressive strength at 91 d. In addition, consistent with the trend of WFS in OPC, high substitution rates of WFS may not be beneficial to the development of compressive strength in AASM. Sithole et al. (9) reported that concrete specimens with 40% slag binder, 30% WFS, and 30% crushed stones in the mixture had the highest unconfined compressive strength at 90 d, i.e., replacement of fine aggregates with more than 30% WFS impaired the unconfined compressive strength of concrete specimens. Bhardwaj et al. (20) also found that in AASM, the mixture with a WFS replacement level of 20% exhibited the highest compressive strength. When the fine aggregate was completely substituted by WFS, the compressive strength was only 45% of the control group. Although the high substitution rate of WFS has a slight deficiency in mechanical properties, it is still implied that WFS shows great potential for application.

For waste waterglass foundry sand (WwFS), a type of WFS bonded by waterglass and hardened by carbon dioxide, the quantity of WwFS awaiting disposal is huge because of its simple preparation procedures. Recently, Fang et al. (21, 22) discovered that one of the essential defects for the decreasing of compressive strength is a poor interface known as sandwich-like interface structure (WwFS-dried waterglass coating-pastes) between WwFS and the surrounding pastes. Although the WwFS interface has an important effect on the performance of concrete containing WwFS, it occupies only a small portion of the entire AASM system, and the dissolution and migration distance of SO_3^{2-} in the dried waterglass layer is quite limited. Therefore, just focusing on improving the bonding of the interface of WwFS is far from sufficient to achieve the goal of enhancing the performance of AASM. In AASM, the formation of binding capacity is dependent on the temperature of WwFS treatment and the type of alkaline activator (23-25). Common alkaline activators such as NaOH, KOH, Na_2SiO_3 and K_2SiO_3 are used to activate slag. Under these highly alkaline conditions, alkaline activators facilitate the dissolution of slag and the reorganization of units such as $(SiO_4)^-$ and $(AlO_4)^-$, which is the process of binder formation in AASM (26, 27). Among them, the combination of NaOH and waterglass works effectively because of their synergistic coupling effect (28, 29). Huang et al. (29) studied that when using both NaOH and liquid waterglass as activators, AASM showed rapid coagulation and high strength. And he also pointed out that the combination of NaOH and waterglass would not affect their respective excitation effects, but rather be mutually reinforcing. Compared to activating the slag with NaOH alone, the addition of waterglass could be beneficial in providing extra SiO_3^{2-} to the pore solution, which reacts with the dissolved ions from slag to form C-(A)-S-H gels with high hydration level (22).

Considering the additional alkaline environment provided by the dried waterglass coating, and its great limitation on the development of strength, this paper proposes utilizing different times and temperatures of the pre-wetted WwFS for preparing AASM. During the hydration process of AAS, the dried waterglass layer needs to absorb water from the pore solution before releasing it as needed to facilitate the transfer of ions such as Al and Si and the polycondensation of oligomers (30). The addition of pre-wetted WwFS allows the water absorption step to be skipped, providing water more directly and efficiently for the hydration of slag. Subsequently, the solubility of waterglass increased with the rise in pre-wetting temperature, leading to the dissolution and release of more SiO_3^{2-} from the wetted waterglass layer into the mixing wa-

ter, activating the bonding potential of the paste matrix in a broader and more homogeneous manner. The dissolved waterglass layer became thinner, weakening the defects of the sandwich structure, and the residual waterglass layer could still play a role in improving the interface. In addition, the waterglass coating of WwFS works as a necessary co-activator to activate slag together with NaOH, resulting in strength enhancement. In this paper, the effect of wet WwFS on the performances of AAS, such as fluidity, compressive strength, flexural strength, scanning electron microscopy (SEM), pore structure and micromechanical properties, was investigated. The significant contribution of this paper is the direct use of wet WwFS as a raw material for the preparation of AAS, unlike other studies focusing on dry WwFS, with a special focus on the interfacial properties between WwFS and paste as well as the waterglass coating in the sandwich-like microstructures. Meanwhile, the effect of the interfacial properties of wet WwFS on the micromechanical properties of AAS was investigated, and the nanoindentation test provided more accurate information for the study of the different phase regions in the microstructure of AAS, which has not yet been addressed in previous studies on dry WwFS. The findings of this research can offer a theoretical foundation for the disposal and utilization of WwFS for application in construction materials, thus contributing to the sustainable development of the city.

2. MATERIALS AND METHODS

2.1. Materials

Shandong Kang Crystal New Material Co., Ltd. provided ground granulated blast slag (GGBS) that met S105 grade standards. The chemical composition, density and BET area of GGBS are shown in Table 1 and the particle size distribution of GGBS is presented in Figure 1. Both the aggregates for AASM and the raw materials for WwFS use quartz sand with a particle size of 380-830 μm and a chemical composition of 99% SiO_2, which is milky white or colourless and translucent. The waterglass, model SP38, has a modulus of about 3.3 and was bought from Jiashan Yourui Refractory Co., LTD. Analytically pure KOH and NaOH were supplied from Tianjin Hengxing Chemical Reagent Manufacturing, Co., Ltd.

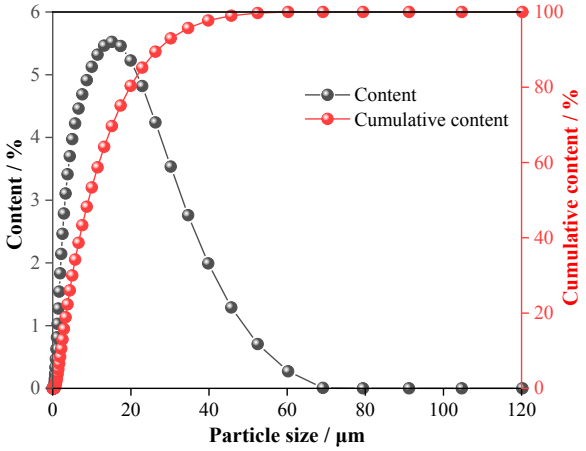

Figure 1. Particle size of GGBS.

2.2. Preparation of WwFS

The production of WwFS is usually higher in industrial production because the use of waterglass in the foundry process is more common. Waterglass is an inorganic cementitious material commonly used as a binder to bind sand grains during the casting process to form the casting model. WwFS are usually subjected to a high temperature thermal field during the casting process, and the shells are heated differently due to the location of the casting, creating a temperature gradient. Using a typical WwFS treated at 100°C guarantees consistency in the treatment temperature of the waterglass layer. According to Fang (22) et al. that real WwFS usually contain more impurities, such as metallic elements and organic matter, which may affect the hydration process of AAS pastes. To ensure that the experiments were controlled, reproducible, and to avoid the influence of impurities such as metallic elements and organics, this study chose not to use

Table 1. The density, BET area, and chemical composition of GGBS / %.

Density (kg/m³)	BET area (m²/g)	Chemical composition / %							
		CaO	SiO_2	Al_2O_3	MgO	Fe_2O_3	TiO_2	K_2O	Other
2800	1535	43.8	26.4	18.3	4.8	1.1	0.9	0.8	3.9

actual waste samples, but to use laboratory-prepared WwFS samples and apply them to the AAS system.

In a Harbor mixer, quartz sand, waterglass, and KOH were mixed together for three minutes at a mass ratio of 100: 5: 2, as per Ref (21). Then, pure CO_2 was injected into the mixture for 10 mins at 5 L/min. After hardening, the mixture was cracked and dried at 100°C for 24 h to prepare WwFS, which was synthesized as shown in Figure 2. Also, WwFS with a particle size of 380-830 μm was selected to keep the same particle size as that of the quartz sand.

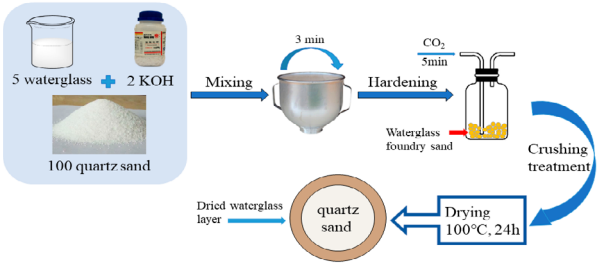

Figure 2. WwFS preparation process.

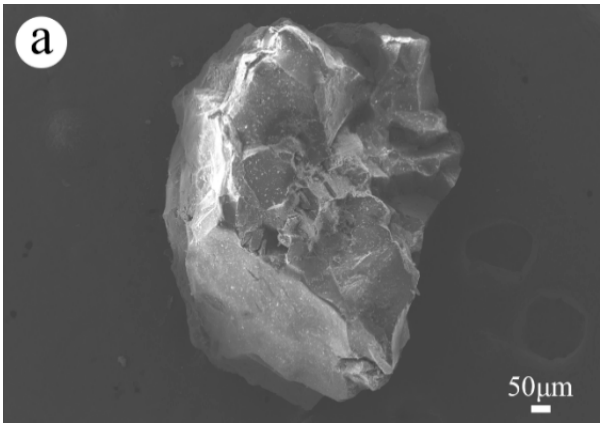

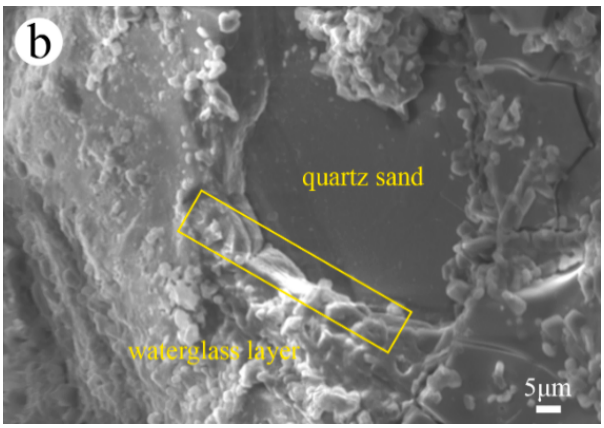

Figure 3. SEM images of (a) quartz sand and (b) WwFS.

As shown in Figure 3b, compared with the sharp-edged and smooth-surfaced quartz sand (Figure 3a), the surface of WwFS is encapsulated with a thicker layer of dry waterglass, which is mainly composed of Na_2CO_3, sodium silicate gel, and a small amount of KOH (31). The width of the waterglass layer is about 1-5 μm. WwFS is composed of quartz sand and the waterglass layer on the surface, so its chemical composition is mainly SiO_2, Na_2SiO_3, Na_2CO_3 and a small amount of KOH. Figure 4 displays the particle size distribution of quartz sand and WwFS analyzed with the Malvern Mastersizer 2000 particle size analyzer. Obviously, the volume of WwFS is higher in the range of 760-1450 μm, while the volume of small (380-760 μm) and large (1450-2000 μm) particle sizes decreases. This may be explained by the mixing, hardening and crushing processes that increase the grain size of small particles and the damage to large sand sizes.

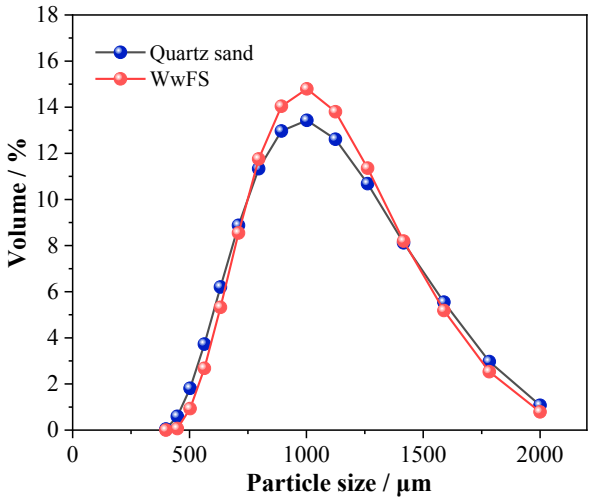

Figure 4. Particle size distribution of quartz sand and WwFS.

The SiO_3^{2-} released from the waterglass coating of WwFS has an important effect on the hydration of AASM. To evaluate the dissolution characteristics of WwFS, the absorbance of Si at 648 nm (32) was tested according to the method of Wang et al (21). Silicate standard solutions of 0, 2, 4, 8, 12, 16 and 20 mg/L were made up using $Na_2SiO_3 \cdot 9H_2O$ and deionized water. Using a 752UV-VIS spectrophotometer, the absorbance of the standard solution was measured. The final standard curve is shown in Equation (1) and presented in Figure 5.

$$A = 0.0313C - 0.0007 \quad [1]$$

Where, C is the concentration of Si and A is the absorbance of the solution.

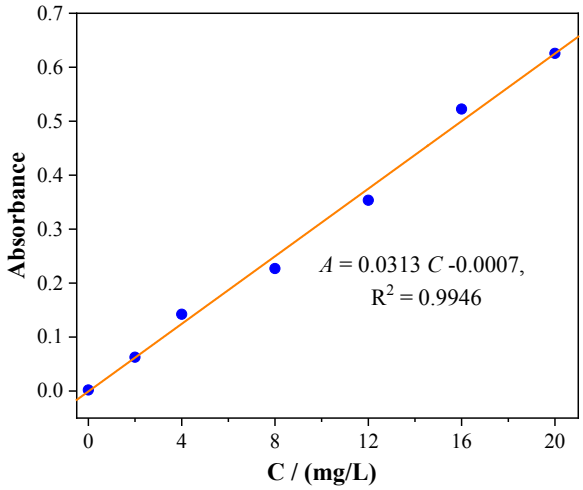

Figure 5. Fitting chart of absorbance of silica at different concentrations.

Table 2. Absorbance and concentration of silicate of WwFS solution.

Time	$WwFS_{20}$		$WwFS_{70}$	
	Absorbance	Concentration of silicate (mg/L)	Absorbance	Concentration of silicate (mg/L)
1h	0.160	5.13	0.386	12.36
3h	0.272	8.72	0.893	28.54
6h	0.325	10.41	1.239	39.62
24h	0.471	15.08	1.319	42.17

Testing solutions were collected at 1, 3, 6, and 24 hours by adding 500 g of $WwFS_{20}$ or $WwSF_{70}$ to 500 mL of deionized water, respectively. The absorbance and silicate concentration of each solution are shown in Table 2. This suggested that the dissolution rate of $WwFS_{70}$ is obviously higher than that of $WwSF_{20}$, which may influence the hydration and mechanical properties of AASM.

2.3. Mix proportion and sample preparation

Six mixtures were designed to explore the influence of the pre-wetting methods of WwFS on AASM performance, 0.55 was the ratio of activator to binder. As shown in Table 3, dried WwFS was used to replace all of the quartz sand in WwFS1. $WwFS_{20}$ and $WwFS_{70}$ represent WwFS immersed in water at 20°C and 70°C, respectively. The last number in the designation denotes the time that WwFS was immersed in water. Also, $WwFS_{70}1$, $WwFS_{70}3$ and $WwFS_{70}6$ can be considered as the experimental groups, and the other three groups as the control groups.

Fresh AAS mortars were prepared by the following process. Initially, NaOH was weighed and added into the water and mixed to exotherm it to room temperature, then WwFS was added and soaked for different times at two temperatures. Dry materials were mixed for three minutes using a Harbor mixer, and then wet materials (water for soaking WwFS and wet WwFS) were added and mixed for 3 mins. Two groups, WwFS0 and WwFS1, directly mixed slag, NaOH solution and sand for three minutes.

Table 3. Mixing proportions of mortars / kg/m³.

Mixtures	GGBS	Water	NaOH	WwFS	Quartz Sand
WwFS0	322.6	177.4	16.64	0	500
WwFS1	322.6	177.4	16.64	500	0
$WwFS_{20}24$	322.6	177.4	16.64	500	0
$WwFS_{70}1$	322.6	177.4	16.64	500	0
$WwFS_{70}3$	322.6	177.4	16.64	500	0
$WwFS_{70}6$	322.6	177.4	16.64	500	0

2.4. Test methods

2.4.1. Fluidity

A STNLD-3 fluidity tester was used to measure the fluidity of AASM in compliance with ASTM C1437 (33). Three samples of each mixture were tested and averages were given.

2.4.2. Compressive strength

According to ASTM C192 (34), fresh mortar was formed in cubic molds of 50 mm size and after vibration the specimens were continuously cured for 3d, 7d and 28d. Finally, three specimens of above age were selected for compressive strength testing.

2.4.3. Flexural strength

The flexural strength of AASM was measured according to ASTM C348 (35). In addition, three sam-

ples were selected at each age, and the test ages were 3, 7, and 28 days, respectively.

2.4.4. Mercury intrusion porosimetry

The pore structure of AASM was analyzed at 28 days using an AutoPore IV 9510 mercury intrusion porosimetry (MIP) analyzer. Test samples were collected from flexural strength testing.

2.4.5. Microstructure analysis

Using a Flex1000 scanning electron microscopy (SEM), the effect of different pre-wetting methods upon the microstructure of AASM was investigated.

2.4.6. Grid nanoindentation

Nanoindentation testing was used to examine the mechanical property of ITZ in the microstructure between WWFS and pastes. First, the samples were cut after testing for flexural strength at 28d and cast into a capsule of 30 mm diameter epoxy resin. The specimens were smoothed with 400, 800 and 1200 grit SiC sandpaper by using a Buehler AutoMet250 Pro polisher, followed by polishing of the specimens with 6 μm, 3 μm and 1 μm diamond suspensions on felt. The KLA-iMicro nanoindenter was used to make 121 indentations in an 11 × 11 grid with a spacing of 10 μm and 231 indentations in an 11 × 21 grid with a spacing of 10 μm. Figure 6 shows the region of 231 indentations covering the aggregate (quartz sand or WwFS) at the bottom of the figure and AAS paste at the top.

The indentation process involved a linear increase in load to 1 mN, achieved through multiple partial unloading steps, followed by a 2 s period of load stability, and eventually a linear decrease to zero over 5 seconds. It was assumed that the Poisson ratio of the prepared specimens was 0.18. To address concerns related to creep, surface roughness, and size effects, each indentation underwent multiple cycles of partial loading and unloading, as recommended in the literature (36). For every indentation, the stiffness was calculated using a specific unloading phase that varied from 95% to 50% of the maximum load. The method for calculating the elastic modulus of the indentation was in accordance with the approach detailed in the literature (37).

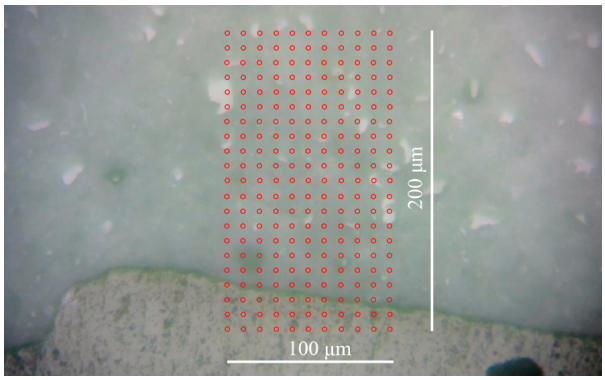

Figure 6. Nanoindentation region of AASM.

3. RESULTS AND DISCUSSION

3.1. Fluidity of mortars

The fluidity of AAS mortars is shown in Figure 7. It is clear that the use of dried WwFS to replace quartz sand reduces the flow of the mortar by 12.7% compared to WwFS0. WwFS is fine and porous and has a larger specific area than quartz sand (12, 38), which increases the water required for particle lubrication and, thus, reduces the fluidity of the mortar. When $WwFS_{20}24$ was added, the fluidity of the AAS mortar increased by 10.4%, in comparison to WwFS1. Since the water absorbed by WwFS can participate in the lubrication between particles (39), the fluidity of the mortar increases. Furthermore, the fluidities of all $WwFS_{70}$-added AAS mortars were lower than that of WwFS1, and the longer the pre-wetting time, the lower the fluidity. Specifically, with increasing the pre-wetting time from 1 h to 6 h, the fluidity decreased by 2.1% to 29.2% compared to WwFS1. The decrease in the fluidity of $WwFS_{70}$-incorporated mortars may indicate that the presence of WwFS accelerated the early hydration of AASM. It could be attributed to the properties of WwFS, as $WwFS_{70}$ is not only rich in hydrophilic silica (40), but also $WwFS_{70}$ is coated with high silica modulus waterglass and KOH, which may release OH^- during the process of hot-water immersion to increase the pH conditions of pore solutions (41). The increased alkalinity in AAS system may accelerate the dissolution process of GGBS and promote the polycondensation of flocculated products (42). Consequently, higher alkaline conditions result in a faster rate of generation of hydration products, which decreases the fluidity of AASM (43).

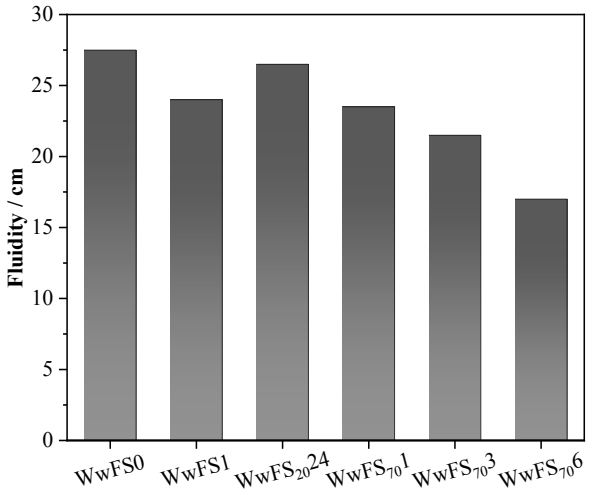

Figure 7. Fluidity of AASM.

3.2. Compressive strength

The compressive strength of AAS mortars is depicted in Figure 8. When WwFS was used to replace all quartz sand, the compressive strength of AASM at all ages increased significantly by 22.1% to 30.8% compared to WwFS0. This may be attributed to the dried waterglass layer that can release a small amount of SiO_3^{2-} into AAS paste, providing an additional source of Si for the formation of hydration products (44). The compressive strength of $WwFS_{20}24$ was reduced at all ages compared to WwFS1. This suggests that the water absorbed by wet WwFS increased the local w/b ratio of AASM (45), although the water released from pre-wetted WwFS may have contributed to the hydration of the slag, but high w/b dominated the negative effect on compressive strength. When incorporating $WwFS_{70}$ into AASM, the compressive strength of AAS mortars was higher than that of WwFS1 and WwFS0 at all ages. As the pre-wetting time increased from 1 h to 6 h, the compressive strength of $WwFS_{70}$ increased by 4.5~10.7% at 3d, 3.7~14.2% at 7d, and 1.3~10.0% at 28d, in comparison with WwFS1. This finding is associated with the dissolution of the waterglass coating with high solubility and the release of ions. Pre-wetting WwFS in hot water dissolved and released more SiO_3^{2-} from the wetted waterglass layer into the mixing water, not just confined around the WwFS, but in a broader and more homogeneous way activating the binding potential of the paste matrix. Moreover, $WwFS_{70}$ could release SiO_3^{2-} and some KOH from the WwFS coating on the quartz particles into the pore solution, working as an auxiliary activator and forming a synergistic activating effect with NaOH on GGBS. Based on previous research by Wang et al. (21), the dried waterglass coating of WwFS could be a primary limiting factor in AASM compressive strength development. However, the waterglass layer of WwFS dissolved in hot water became thinner, weakening the defects of the sandwich structure, while the residual waterglass layer still played a role in improving the bonding between aggregate and paste (46, 47). Hence, more hydration products could be generated in the interfacial transition zone (ITZ), resulting in a denser ITZ between WwFS and the surrounding paste, thus increasing the compressive strength of AASM.

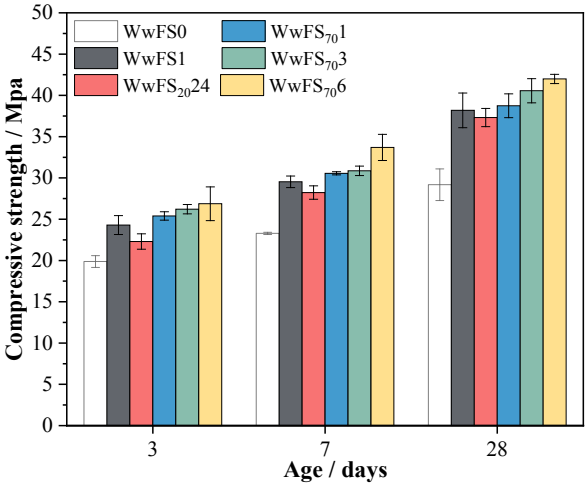

Figure 8. Compressive strength of AASM.

3.3. Flexural strength

The flexural strength of AAS mortars is presented in Figure 9. It is clear that the development trend of flexural strength is similar to that of compressive strength of AAS mortars with different pre-wetted WwFS treatment methods. The flexural strength of WwFS1 is higher than that of WwFS0 by approximately 16.2~20.0% at all ages. Although the flexural strength of $WwFS_{20}24$ is lower than that of WwFS1 due to its high w/b, it is still higher than the flexural strength of WwFS0. In addition, the flexural strength of mortar at all ages increases with the increase of soaking time when the pre-wetting temperature of treated WwFS is kept at 70°C. At 28d, the flexural strength of $WwFS_{70}$ is increased by 3.1~18.3% compared to WwFS0, where $WwFS_{70}6$ possesses the highest flexural strength. The increase in flexural strength is attributed to the waterglass coating on $WwFS_{70}$, which is highly soluble as shown in Table 2. WwFS can release SiO_3^{2-} into the pore solution around the paste, providing additional Si species for the gener-

ation of hydration products (48). As a result, more stress-bearing hydration products can be produced and the microstructure of AAS can be densified, resulting in higher flexural strength.

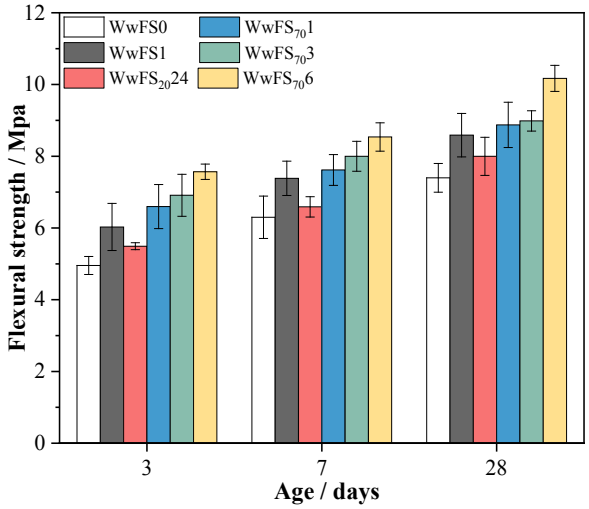

Figure 9. Flexural strength of AASM.

3.4. Pore structure

Figure 10a presents the pore structure of AAS mortars. The pore size distributions are very similar for all groups, with a distinct single peak around 10 nm and a flat profile after 100 nm. After adding WwFS1, the peak increased obviously compared to WwFS0. This may be associated with the inherent sandwich-like structure of WwFS, where the interface between the paste and aggregate changes from dual to ternary, leading to additional pores in the microstructure system (21). The mortar with the addition of WwFS$_{20}$24 was similar to that of WwFS1, which suggests that room temperature pre-wetting for 24 h did not improve the pore structure. The free water and waterglass released by WwFS$_{20}$24 could probably produce a denser ITZ, but the effect is rather weakened by the locally high w/b. By contrast, with the increase of hot water pre-wetting time, the peak of WwFS$_{70}$ exhibited a tendency to gradually decrease and move to the left, indicating that WwFS$_{70}$ refined the pore structure of AASM. Generally, pores smaller than 10 nm mainly consist of gel pores and pores between gel units, the lowest peak of WwFS$_{70}$6 means that soaking WwFS in hot water results in tighter connection between generated gel (49-52). Moreover, it is also possible that waterglass has entered the paste, generating extra hydration products that fill the pores and cracks, further densifying the ITZ.

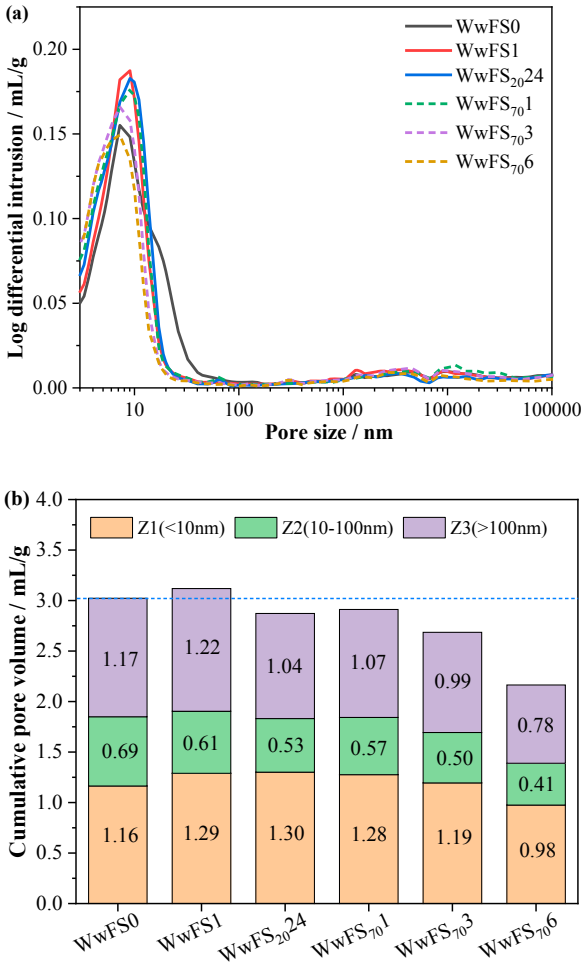

Figure 10. Pore structure of 28d AASM: (a) pore sizes distribution; (b) cumulative pore volume.

Figure 10b further shows the cumulative volume of pores in the three zones. It is evident that replacing quartz sand with WwFS increased the total pore volume of the mortar by 3.3%, indicating that the sandwich structure introduced more pores into AASM. Incorporating pre-wetted WwFS not only reduced the total porosity and macro pores volume, but also optimized the gel pores and capillary pores volume. However, the improvement in the pore structure of mortars by pre-wetting WwFS at 20°C was limited, with a slight reduction in the total porosity of mortars containing WwFS$_{20}$24 compared to WwFS1. With the addition of WwFS$_{70}$, the volumes of all three pore size zones decreased, especially the total porosity of WwFS$_{70}$6 decreased by 30.4% compared to that of WwFS1. Therefore, since the refined pore structure could be produced in AASM using WwFS$_{70}$, the hypothesis about the auxiliary activation of slag by WwFS$_{70}$ is further substantiated.

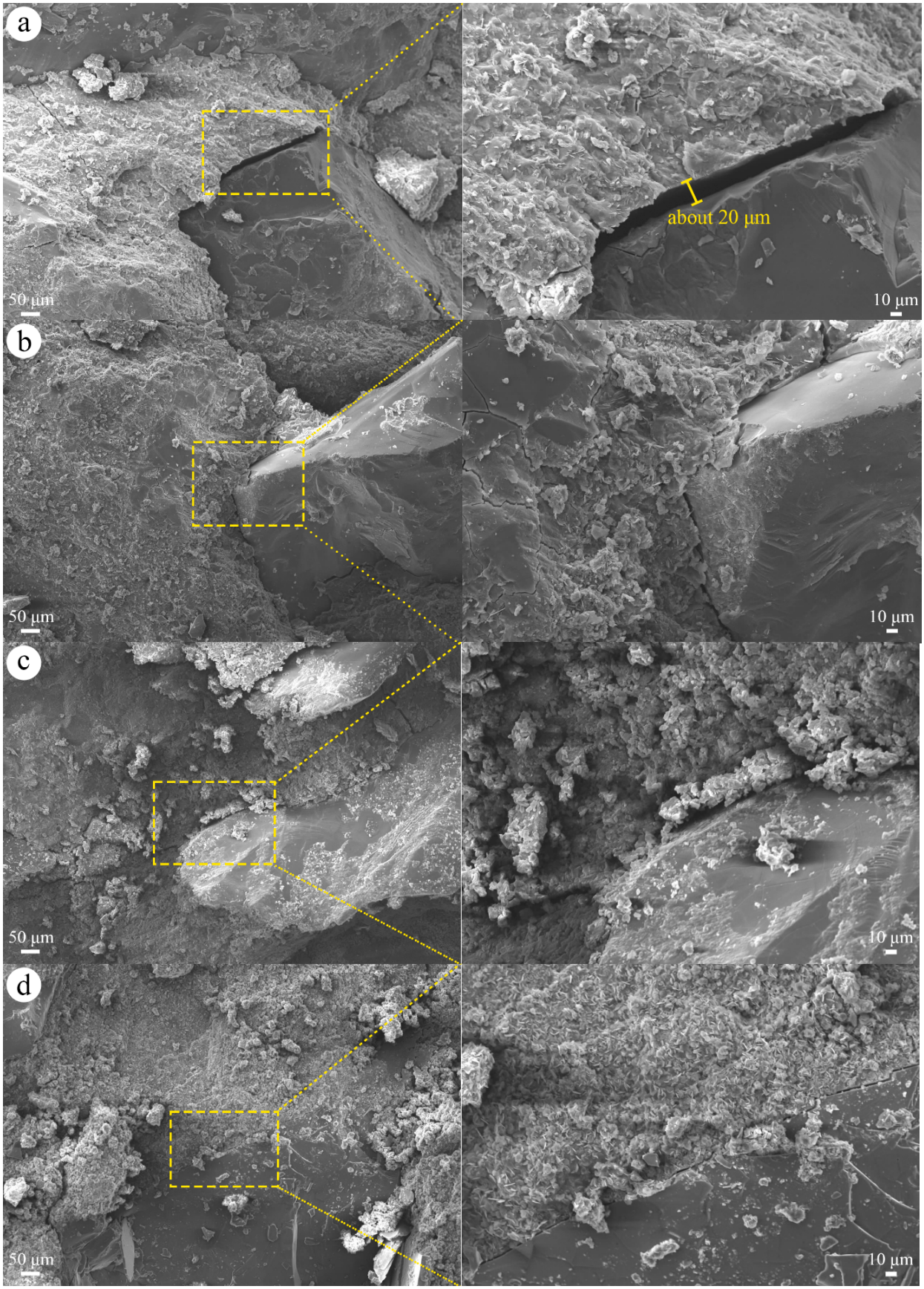

Figure 11. SEM images of 28d AASM: (a) WwFS0; (b) WwFS1; (c) $WwFS_{20}24$; (d) $WwFS7_{0}1$; (e) $WwFS_{70}6$.

3.5. Microstructure analysis

The typical SEM images of 28d AASM are shown in Figure 11. From Figure 11(a), cracks with a width as high as 20 μm were found between the quartz sand and the surrounding paste, which indicates that the interface is a typical physical interface with poor bonding. After substituting quartz sand with WwFS, the cracks between WwFS1 and AAS paste were clearly narrowed. Since the layer of dried waterglass on the surface of WwFS1 may dissolve into the surrounding paste in small amounts, it promoted the hydration of slag, leading to an enhanced bonding effect between WwFS1 and AAS paste. The paste around $WwFS_{20}24$ is loose and porous, as shown in Figure 11(c), attributed to a significant local increase in w/b near WwFS. This results in the deterioration of the microstructure (53), consistent with the decrease in compressive strength of $WwFS_{20}24$ in Figure 8. In contrast, AASM with the addition of $WwFS_{70}1$ exhibited a large number of hydration products in the microstructure, such as C-(A)-S-H gels. Dissolved SiO_3^{2-} and KOH from the hot water-soaked waterglass layer could be released into the mixing water as a source of coactivator in addition to NaOH. Moreover, the pre-wetted waterglass coating could function as reactive aggregates, with the dissolution and permeation of SiO_3^{2-} and some KOH facilitating the hydration of the surrounding slag particles, producing additional hydration products. The enhanced dense ITZ structural layer was observed in $WwFS_{70}6$ with tight interfaces and no cracks generated, as shown in

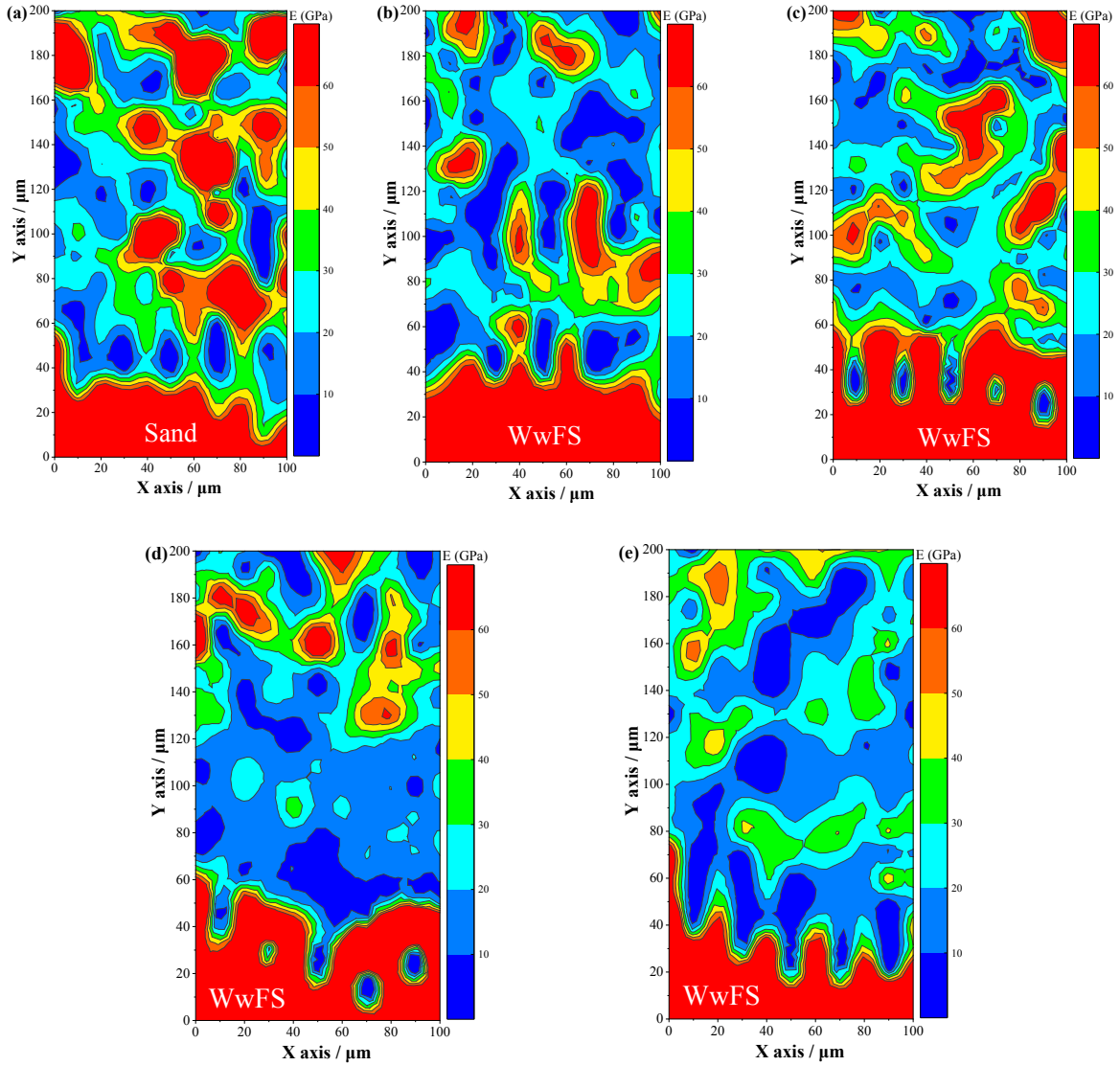

Figure 12. Contour mappings of the elastic modulus in AAS interface: (a) WwFS0; (b) WwFS1; (c) $WwFS_{20}24$; (d) $WwFS_{70}1$; (e) $WwFS_{70}6$.

Figure 11(e). In conclusion, the improved bonding between WwFS and surrounding paste by hot water pre-wetting of WwFS can be confirmed, consequently influencing the compressive strength and pore structure of AAS mortar.

3.6. Nanoindentation analysis (interface and paste around WwFS)

Figure 12 shows the contour mapping of the elastic modulus of AAS mixtures determined by nano-indentation method, respectively. The average elastic modulus of AASM along the Y axis in Figure 12 was calculated to investigate the variations in ITZ properties after incorporating pre-wetted WwFS, as shown in Figure 13. There is no weak zone between the quartz sand and paste, and the elastic modulus is approximately 30~50 GPa. Since the dried waterglass layer may cause the discontinuity of the interface structure, a weak transition zone was found in WwFS1. The ITZ thickness of AAS mortar with the addition of WwFS is about 60 μm. For $WwFS_{20}24$, ITZ has the lowest elastic modulus. However, the ITZ with the addition of $WwFS_{70}$ was enhanced with an increase in elastic modulus, and in particular, the elastic modulus of ITZ with $WwFS_{70}6$ tended to be closer to that of WwFS0. This implies that hot water immersion treatment of WwFS did promote slag hydration, generating more hydration products in the interface. Meanwhile, these results further proved that $WwFS_{70}6$ can achieve better bonding between AASM matrix and aggregate, and also contribute to the strength of mortars.

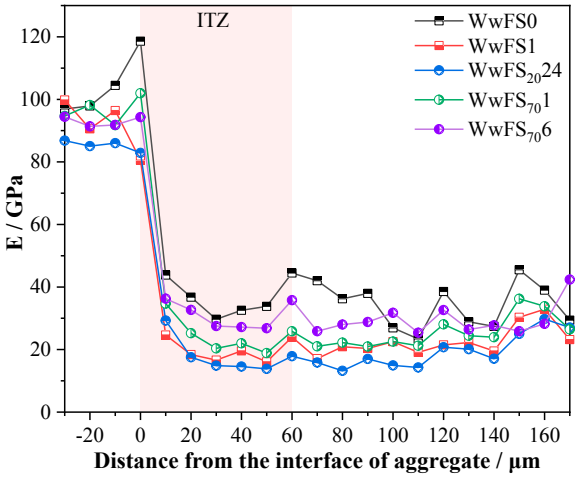

Figure 13. Distributions of averaged elastic modulus in ITZ.

Figure 14 presents the contour mapping of elastic modulus of pastes around AAS aggregates. The red areas represent unhydrated GGBS or aggregates with an elastic modulus more than 60 GPa (54), while the areas less than 60 GPa are considered to be hydration products. In Figs. 14d and 14e, the red (>60 GPa) areas are significantly decreased and the cyan (20~30 GPa) and green (30~40 GPa) areas are increased, which

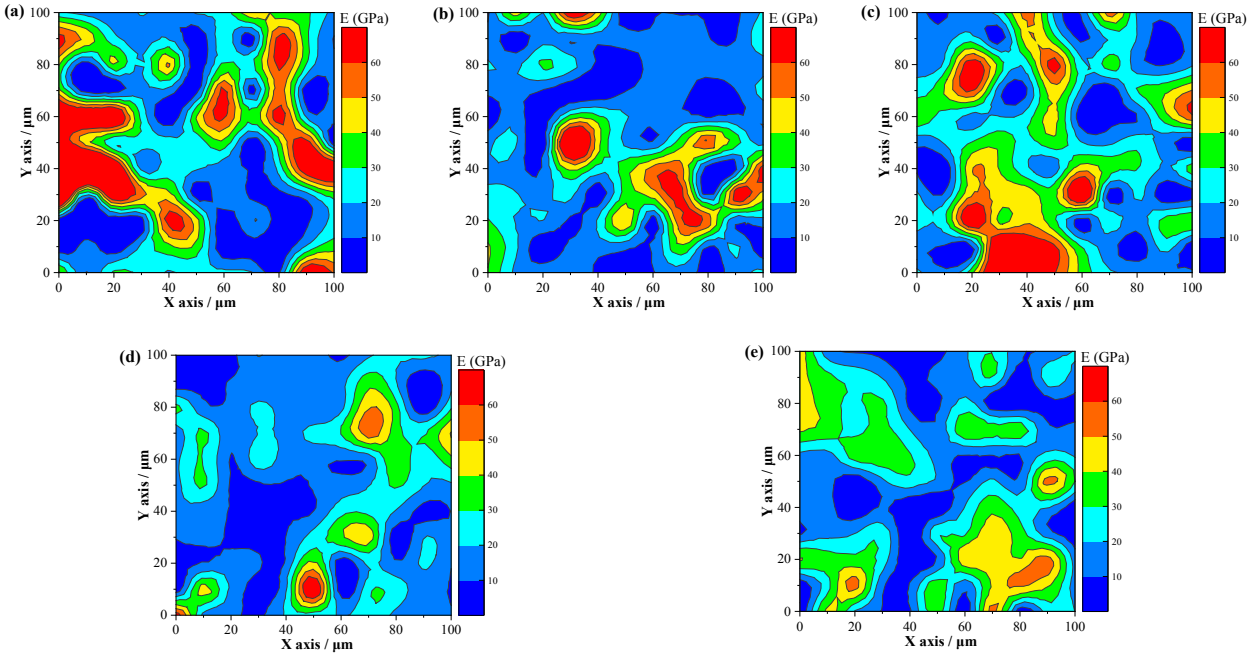

Figure 14. Nanoindentation results of AASM pastes around WwFS: (a), (b), (c) elastic modulus mapping for WwFS0, WwFS1, WwFS2024, WwFS701 and WwFS706.

suggests that WwFS$_{70}$6-added mortars had a higher degree of hydration with less unhydrated GGBS.

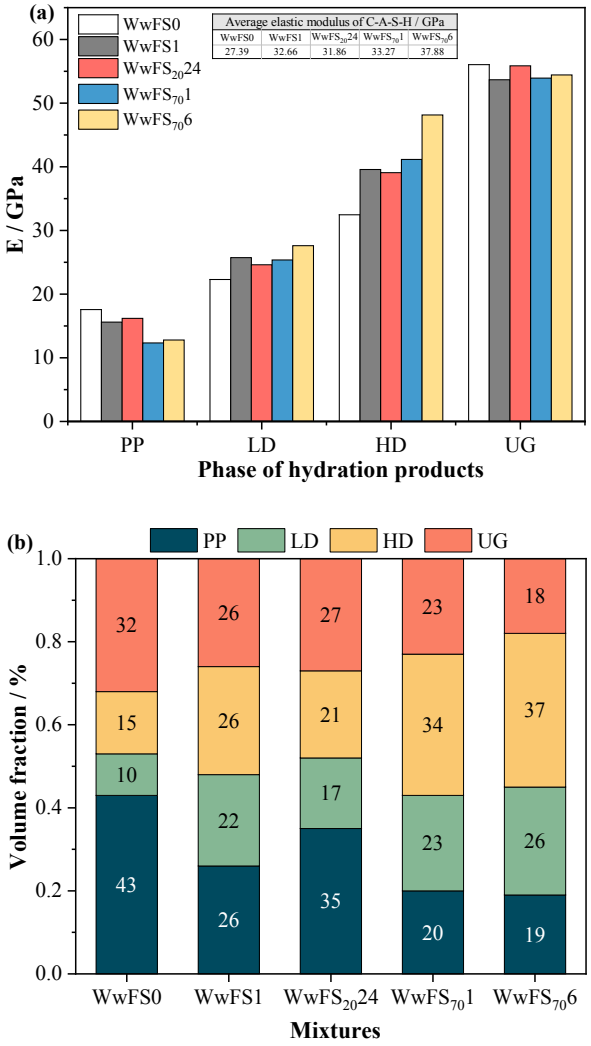

Figure 15. Comparison of indentation properties of four different phases of hydrates for AASM: (a) Elastic modulus; and (b) Volume fraction.

Figure 15 illustrates the deconvolution results of elastic modulus and volume fraction of pastes around AAS aggregates. According to previous studies, the elastic modulus was divided into four stages in order from low to high, i.e., porous phase (PP), low-density C-A-S-H (LD), high-density C-A-S-H (HD) and unreacted GGBS (UG). The average elastic modulus of C-A-S-H for each mixture is presented in the inset table in Figure 15a. After replacing quartz sand with WwFS, the average elastic modulus of both LD and HD was higher than that of WwFS0. Compared to WwFS1, the C-A-S-H average elastic modulus is increased for all of WwFS$_{70}$, although WwFS$_{20}$24 is slightly lower. The average elastic modulus of C-A-S-H increased from 32.66 GPa for WwFS1 to 37.88 GPa for WwFS$_{70}$6, indicating that the addition of WwFS$_{70}$6 densified the microstructure of the hydration products. In Figure 15b, the hydration products with the largest volume fraction in WwFS$_{70}$1 and WwFS$_{70}$6 are both HD. WwFS$_{70}$6 shows a decrease in PP volume fraction from 26% to 19% and an increase in HD volume fraction from 26% to 37% compared to WwFS1, suggesting that WwFS$_{70}$6 promotes the formation of more HD in AAS. The above findings further demonstrate the synergistic effect on activating the slag between NaOH and sodium silicate dissolved into the mixing water, which contributes to improving the compressive strength of AAS mortars, consistent with the results of MIP.

4. CONCLUSIONS

This study investigates the replacement of quartz sand by WwFS at two different pre-wetting methods (24 h pre-wetting at 20°C and 1~6 h pre-wetting at 70°C) and compares their performances with those of added quartz sand and dried WwFS mortars. The experimental results demonstrated that the addition of dried WwFS resulted in lower fluidity and higher compressive strength than WwFS0 due to the dried waterglass layer that can release a small amount of SiO_3^{2-} into AAS paste. Although the pre-wetted WwFS improved fluidity, the increase in local w/b led to a decrease in the compressive strength of WwFS$_{20}$24. In contrast, the addition of WwFS$_{70}$ achieved higher compressive and flexural strengths and denser pore structure than WwFS1. On the one hand, the solubility of waterglass increased with increasing pre-wetting temperature, leading to the dissolution and release of more SiO_3^{2-} from the wetted waterglass layer into the mixing water, which activated the bonding potential of the paste matrix in a broader and more homogeneous manner and promoted the generation of additional hydration products. As the pre-wetting time increased from 1 h to 6 h, the compressive strength of WwFS$_{70}$ increased by 4.5~10.7% at 3d, 3.7~14.2% at 7d, and 1.3~10.0% at 28d, in comparison with WwFS1. On the other hand, the dissolved waterglass layer becomes thinner, weakening the defects of the sandwich structure, while the residual waterglass layer still plays a role in improving the interface. The hydration of the slag was improved in WwFS$_{70}$6-added mortars, with fewer and smaller unhydrated slag particles around WwFS, and no obvious ITZ in the microstructure.

Funding Sources

This work was funded by the National Natural Science Foundation of China (52008003), Outstanding Youth Project of Natural Science Research in Universities of Anhui Province (23AH030043), National Key Research and Development Plan (2021YFB3401504).

Authorship contribution statement

Xin Shen: Investigation, Methodology, Writing-original draft.

Peiyuan Chen: Conceptualization, Supervision, Writing – review & editing.

Shangkun Li: Investigation.

Yonghui Wang: Investigation.

Shuimu Hu: Investigation.

Chunning Pei: Investigation.

Jiankai Xie: Investigation.

Declaration of competing interest

The authors of this article declare that they have no financial, professional or personal conflicts of in-terest that could have inappropriately influenced this work.

REFERENCES

1. Ashish DK, Verma SK. 2021. Robustness of self-compacting concrete containing waste foundry sand and metakaolin: A sustainable approach. J. Hazard Mater. 401: 123329. https://doi.org/10.1016/j.jhazmat.2020.123329
2. Dyer PPOL, de Lima MG, Klinsky LMG, Silva SA, Coppio GJL. 2018. Environmental characterization of Foundry Waste Sand (WFS). in hot mix asphalt (HMA. mixtures. Constr. Build. Mater. 171:474-484. https://doi.org/10.1016/j.conbuildmat.2018.03.151
3. Parashar A, Aggarwal P, Saini B, Aggarwal Y, Bishnoi S. 2020. Study on performance enhancement of self-compacting concrete incorporating waste foundry sand. Constr. Build. Mater. 251:118875. https://doi.org/10.1016/j.conbuildmat.2020.118875
4. Kaur G, Siddique R, Rajor A. 2012. Properties of concrete containing fungal treated waste foundry sand. Constr. Build. Mater. 29:82-87. https://doi.org/10.1016/j.conbuildmat.2011.08.091
5. Siddique R, Schutter Gd, Noumowe A. 2009. Effect of used-foundry sand on the mechanical properties of concrete. Constr. Build. Mater. 23(2):976-980. https://doi.org/10.1016/j.conbuildmat.2008.05.005
6. Mashifana T, Sithole T. 2020. Recovery of silicon dioxide from waste foundry sand and alkaline activation of desilicated foundry sand. J. Sustainable Metall. 6(4):700-714. https://doi.org/10.1007/s40831-020-00303-5
7. Ferrazzo ST, Araújo MTd, Bruschi GJ, Chaves HM, Korf EP, Consoli NC. 2023. Mechanical and environmental behavior of waste foundry sand stabilized with alkali-activated sugar cane bagasse ash-eggshell lime binder. Constr. Build. Mater. 383:131313. https://doi.org/10.1016/j.conbuildmat.2023.131313
8. Mavroulidou M, Lawrence D. 2018. Can waste foundry sand fully replace structural concrete sand?. J. Mater. Cycles Waste Manage. 21(3):594-605. https://doi.org/10.1007/s10163-018-00821-1
9. Sithole NT, Tsotetsi NT, Mashifana T, Sillanpää M. 2022. Alternative cleaner production of sustainable concrete from waste foundry sand and slag. J. Cleaner Prod. 336:130399. https://doi.org/10.1016/j.jclepro.2022.130399
10. Sawai H, Rahman IMM, Fujita M, Jii N, Wakabayashi T, Begum ZA, Maki T, Mizutani S, Hasegawa H. 2016. Decontamination of metal-contaminated waste foundry sands using an EDTA–NaOH–NH_3 washing solution. Chem. Eng. J. 296:199-208. https://doi.org/10.1016/j.cej.2016.03.078
11. Park CL, Kim BG, Yu Y. 2012. The regeneration of waste foundry sand and residue stabilization using coal refuse. J. Hazard. Mater. 203-204:176-182. https://doi.org/10.1016/j.jhazmat.2011.11.100
12. Ahmad J, Aslam F, Zaid O, Alyousef R, Alabduljabbar H. 2021. Mechanical and durability characteristics of sustainable concrete modified with partial substitution of waste foundry sand. Struct. Concr. 22(5):2775-2790. https://doi.org/10.1002/suco.202000830
13. Iloh P, Fanourakis G, Ogra A. 2019. Evaluation of physical and chemical properties of South African Waste Foundry Sand (WFS). for Concrete Use, Sustainability. 11(1):193. https://doi.org/10.3390/su11010193
14. Manoharan T, Laksmanan D, Mylsamy K, Sivakumar P, Sircar A. 2018. Engineering properties of concrete with partial utilization of used foundry sand. Waste Manage. (Oxford). 71:454-460. https://doi.org/10.1016/j.wasman.2017.10.022
15. Prabhu GG, Hyun JH, Kim YY. 2014. Effects of foundry sand as a fine aggregate in concrete production. Constr. Build. Mater. 70:514-521. https://doi.org/10.1016/j.conbuildmat.2014.07.070
16. Guney Y, Sari YD, Yalcin M, Tuncan A, Donmez S. 2010. Re-usage of waste foundry sand in high-strength concrete. Waste Manage. (Oxford). 30(8-9):1705-1713. https://doi.org/10.1016/j.wasman.2010.02.018
17. Mynuddin S, Mohan M, Reddy TI, Pratik Reddy N. 2018. Strength behavior of concrete produced with foundry sand as fine aggregate replacement. Int. J. Mod. Trends Eng. Sci. 5(8):3476-3480. https://doi.org/10.13140/RG.2.2.29829.91367/1
18. Martins MA, Barros RM, da Silva LRR, dos Santos VC, Lintz RC, Gachet LA, de Lourdes Melo M, Martinez CB. 2022. Durability indicators of high-strength self-compacting concrete with marble and granite wastes and waste foundry exhaust sand using electrochemical tests. Constr. Build. Mater. 317:125907. https://doi.org/10.1016/j.conbuildmat.2021.125907
19. Sabour MR, Derhamjani G, Akbari M. 2022. Mechanical, durability properties, and environmental assessment of geopolymer mortars containing waste foundry sand. Environ. Sci. Pollut. Res. Int. 29(16):24322-24333. https://doi.org/10.1007/s11356-021-17692-z
20. Bhardwaj B, Kumar P. 2019. Comparative study of geopolymer and alkali activated slag concrete comprising waste foundry sand. Constr. Build. Mater. 209:555-565. https://doi.org/10.1016/j.conbuildmat.2019.03.107
21. Wang C, Chen P, Xu Y, Zhang L, Luo Y, Li J, Wang Y. 2022. Investigation on the utilization of spent waterglass foundry sand into $Ca(OH)_2$-activated slag materials considering the coating layer of dried waterglass. Constr. Build. Mater. 329:127180. https://doi.org/10.1016/j.conbuildmat.2022.127180
22. Fang J, Xie J, Wang Y, Tan W, Ge W. 2023. Alkali-activated slag materials for bulk disposal of waste waterglass foundry sand: A promising approach. J. Build. Eng. 63(Part A):105422. https://doi.org/10.1016/j.jobe.2022.105422
23. Fernández Jiménez A, Palomo JG, Puertas F. 1999. Alkali-activated slag mortars: Mechanical strength behaviour. Cem.

Concr. Res. 29(8):1313-1321. https://doi.org/10.1016/S0008-8846(99)00154-4
24. Collins FG, Sanjayan JG. 1999. Workability and mechanical properties of alkali activated slag concrete. Cem. Concr. Res. 29(3):455-458. https://doi.org/10.1016/S0008-8846(98)00236-1
25. Bakharev T, Sanjayan JG, Cheng Y. 1999. Alkali activation of Australian slag cements. Cem. Concr. Res. 29(1):113-120. https://doi.org/10.1016/S0008-8846(98)00170-7
26. Abubakr AE, Soliman AM, Diab SH. 2020. Effect of activator nature on the impact behaviour of Alkali-Activated slag mortar. Constr. Build. Mater. 257:119531. https://doi.org/10.1016/j.conbuildmat.2020.119531
27. Kai MF, Li G, Yin BB, Akbar A. 2023. Aluminum-induced structure evolution and mechanical strengthening of calcium silicate hydrates: an atomistic insight. Constr. Build. Mater. 393:132120. https://doi.org/10.1016/j.conbuildmat.2023.132120
28. Zhang Z, Jia Y, Liu J. 2022. Influence of different parameters on the performance of alkali-activated slag/fly ash composite system. Materials. 15(8):2714. https://doi.org/10.3390/ma15082714
29. Jin L, Huang G, Li Y, Zhang X, Ji Y, Xu Z. 2021. Positive influence of liquid sodium silicate on the setting time, polymerization, and strength development mechanism of MSWI bottom ash alkali-activated mortars. Materials. 14(8):1927. https://doi.org/10.3390/ma14081927
30. Li W, Lemougna PN, Wang K, He Y, Tong Z, Cui X. 2017. Effect of vacuum dehydration on gel structure and properties of metakaolin-based geopolymers. Ceram. Int. 43(16):14340-14346. https://doi.org/10.1016/j.ceramint.2017.07.190
31. Qiu Y, Pan H, Zhao Q, Zhang J, Zhang Y, Guo W. 2022. Carbon dioxide-hardened sodium silicate-bonded sand regeneration using calcium carbide slag: The design and feasibility study. J. Environ. Chem. Eng. 10(3):107872. https://doi.org/10.1016/j.jece.2022.107872
32. Jiang Z, Li J, Li W. 2019. Preparation and characterization of autolytic mineral microsphere for self-healing cementitious materials. Cem. Concr. Compos. 103:112-120. https://doi.org/10.1016/j.cemconcomp.2019.04.004
33. ASTM C1437. 2020. Standard test mrthod for flow of hydraulic cement mortar. ASTM International, West Conshohocken, PA. Retrieved from https://www.astm.org/.
34. Burciaga Díaz O, Betancourt Castillo I. 2018. Characterization of novel blast-furnace slag cement pastes and mortars activated with a reactive mixture of MgO-NaOH. Cem. Concr. Res. 105:54-63. https://doi.org/10.1016/j.cemconres.2018.01.002
35. ASTM C348-18. 2018. Standard test method for flexural strength of hydraulic-cement mortars. ASTM International, West Conshohocken, PA. Retrieved from https://www.astm.org.
36. Mondal P. 2008. Nanomechanical properties of cementitious materials. Northwestern University ProQuest Dissertations Publishing.
37. Xie J, Chen P, Li J, Xu Y, Fang Y, Wang A, Wang J. 2022. Directly upcycling copper mining wastewater into a source of mixing water for the preparation of alkali-activated slag materials. Process Saf. Environ. Prot. 168:362-371. https://doi.org/10.1016/j.psep.2022.10.011
38. Martins MAB, da Silva LRR, Ranieri MGA, Barros RM, Dos Santos VC, Goncalves PC, Rodrigues MRB, Lintz RCC, Gachet LA, Martinez CB, Melo M. 2021. Physical and chemical properties of waste foundry exhaust sand for use in self-compacting concrete. Materials. 14(19):5629. https://doi.org/10.3390/ma14195629
39. Ashish DK, Verma SK, Ju M, Sharma H. 2023. High volume waste foundry sand self-compacting concrete – Transitioning industrial symbiosis. Process Saf. Environ. Prot. 173:666-692. https://doi.org/10.1016/j.psep.2023.03.028
40. Şahmaran M, Lachemi M, Erdem TK, Yücel HE. 2010. Use of spent foundry sand and fly ash for the development of green self-consolidating concrete. Mater. Struct. 44(7):1193-1204. https://doi.org/10.1617/s11527-010-9692-7
41. Liu Q, Zhang J, Su Y, Lü X. 2021. Variation in polymerization degree of C-A-S-H gels and its role in strength development of alkali-activated slag binders. Journal of Wuhan University of Technology-Mater. Sci. Ed. 36(6):871-879. https://doi.org/10.1007/s11595-021-2281-z
42. Cihangir F, Ercikdi B, Kesimal A, Deveci H, Erdemir F. 2015. Paste backfill of high-sulphide mill tailings using alkali-activated blast furnace slag: Effect of activator nature, concentration and slag properties. Miner. Eng. 83:117-127. https://doi.org/10.1016/j.mineng.2015.08.022
43. Zhu Z, Xu X, Liu R, Liu P, Tang H, Gong Y, Zhang C, Li X, Liu Y, Bai J, Chen M. 2023. Feasibility study of highly alkaline biomass ash to activate alkali-activated grouts. Constr. Build. Mater. 393:132067. https://doi.org/10.1016/j.conbuildmat.2023.132067
44. Kai MF, Sanchez F, Hou DS, Dai JG. 2023. Nanoscale insights into the interfacial characteristics between calcium silicate hydrate and silica. Appl. Surf. Sci. 616:156478. https://doi.org/10.1016/j.apsusc.2023.156478
45. Liu K, Yu R, Shui Z, Yi S, Li X, Ling G, He Y. 2020. Influence of external water introduced by coral sand on autogenous shrinkage and microstructure development of Ultra-High Strength Concrete (UHSC). Constr. Build. Mater. 252:119111. https://doi.org/10.1016/j.conbuildmat.2020.119111
46. Basar HM, Deveci Aksoy N. 2012). The effect of waste foundry sand (WFS. as partial replacement of sand on the mechanical, leaching and micro-structural characteristics of ready-mixed concrete. Constr. Build. Mater. 35:508-515. https://doi.org/10.1016/j.conbuildmat.2012.04.078
47. Ganesh Prabhu G, Hyun JH, Kim YY. 2014. Effects of foundry sand as a fine aggregate in concrete production. Constr. Build. Mater. 70:514-521. https://doi.org/10.1016/j.conbuildmat.2014.07.070
48. Puertas F, Palacios M, Manzano H, Dolado J, Rico A, Rodríguez J. 2011. A model for the CASH gel formed in alkali-activated slag cements. J. Eur. Ceram. Soc. 31(12):2043-2056. https://doi.org/10.1016/j.jeurceramsoc.2011.04.036
49. Chen P, Wang J, Wang L, Xu Y. 2019. Perforated cenospheres: A reactive internal curing agent for alkali activated slag mortars. Cem. Concr. Compos. 104:103351. https://doi.org/10.1016/j.cemconcomp.2019.103351
50. Hu X, Shi C, Shi Z, Zhang L. 2019. Compressive strength, pore structure and chloride transport properties of alkali-activated slag/fly ash mortars. Cem. Concr. Compos. 104:103392. https://doi.org/10.1016/j.cemconcomp.2019.103392
51. Zhang Z, Zhu Y, Zhu H, Zhang Y, Provis JL, Wang H. 2019. Effect of drying procedures on pore structure and phase evolution of alkali-activated cements. Cem. Concr. Compos. 96:194-203. https://doi.org/10.1016/j.cemconcomp.2018.12.003
52. Ran B, Omikrine Metalssi O, Fen Chong T, Dangla P, Li K. 2023. Pore crystallization and expansion of cement pastes in sulfate solutions with and without chlorides. Cem. Concr. Res. 166:107099. https://doi.org/10.1016/j.cemconres.2023.107099
53. Hu X, Shi C, Li J, Wu Z. 2021. Chloride migration in cement mortars with ultra-low water to binder ratio. Cem. Concr. Compos. 118:103974. https://doi.org/10.1016/j.cemconcomp.2021.103974
54. Ahmad MR, Qian L, Fang Y, Wang A, Dai J. 2023. A multiscale study on gel composition of hybrid alkali-activated materials partially utilizing air pollution control residue as an activator. Cem. Concr. Compos. 136:104856. https://doi.org/10.1016/j.cemconcomp.2022.104856